Annu. Rev. Mater. Sci. 1999. 29:117–48

SCANNING SQUID MICROSCOPY

John R. Kirtley
IBM T. J. Watson Research Center, Yorktown Heights, New York 10598;
e-mail: kirtley@watson.ibm.com

John P. Wikswo, Jr.
Department of Physics and Astronomy, Vanderbilt University, Nashville,
Tennessee 37235; e-mail: wikswojp@ctrvax.vanderbilt.edu

KEY WORDS: magnetic, inspection, superconductivity, defects, corrosion

ABSTRACT

The scanning SQUID microscope (SSM) is a powerful tool for imaging magnetic fields above sample surfaces. It has the advantage of high sensitivity and bandwidth and the disadvantages of relatively modest spatial resolution and the requirement of a cooled SQUID sensor. We describe the various implementations of this type of instrument and discuss a number of applications, including magnetic imaging of short circuits in integrated circuits, corrosion currents in aluminum, and trapped flux in superconductors.

INTRODUCTION

There are many techniques for imaging sample magnetic fields. In addition to superconducting quantum interference device (SQUID) magnetometers, which are the subject of this review, widely used techniques include scanning Hall bar microscopy (1), scanning magnetoresistive microscopy (2), magnetic force microscopy (3), magneto-optical imaging (4), scanning electron microscopy with polarization analysis (SEMPA) (5), electron holography (6), inductive pickups using a video head (7), and decoration techniques (8). Each has its own advantages and disadvantages. For instance, micron-sized Hall bars have a flux sensitivity comparable to SQUIDs (9) and do not have to be operated at as low a temperature. However, the field sensitivity of SQUIDs increases linearly with the pickup area, whereas the field sensitivity of Hall bars is nearly independent of area. Therefore, SQUIDs rapidly become more sensitive than Hall bars

0084-6600/99/0801-0117$08.00

with increasing pickup area. Furthermore, Hall bars are much more sensitive to pressure and charging effects than are SQUIDs. Micron-sized magnetoresistive sensors also have flux sensitivity comparable to SQUIDs. However, they are typically operated with a dc current of several mA, which means that the magnetic field and the heat they generate can perturb the sample, especially for superconducting applications. Magnetic force microscopy typically measures the gradient of the magnetic field, which can complicate interpretations of the measurements, and their sensitivity to fields from objects larger than micron-sized is orders of magnitude lower than that of SQUIDs. Moreover, the field generated by the ferromagnetic material on the scanning tip can perturb the sample. Electron holography can image small fields at video rates but requires thinned samples. Differential phase contrast Lorentz microscopy, which measures the in-phase derivative of the phase of the electron beam, is sensitive to magnetization within the sample rather than just the field outside (10). As should already be evident, the phase space for magnetic imaging is multidimensional and includes sensitivity, spatial resolution, frequency response, linearity, and stability. Other factors include the required proximity of the detector to the source, the detection of fields versus gradients, the need to operate in an externally applied field, the ability to reject external noise or the applied field, the ability to make measurements without perturbing the sample, and the required operating temperature of both the sample and the sensor.

SQUID MICROSCOPES

Ever since their introduction in the 1970s, SQUID magnetometers have been incorporated into a wide variety of experiments to measure weak magnetic fields. Laboratory and commercial instruments have utilized SQUIDs as the primary sensing element of accelerometers, ammeters, ELF and RF receivers, gravimeters, gravity wave antennas, impedance bridges, magnetic resonance detectors, susceptometers, thermometers, voltmeters, etc (11, 12). Typically with such systems, a single SQUID is used to measure a single physical quantity as a function of time, often with the sample contained within a SQUID pickup coil that is heavily shielded from outside magnetic noise. Magnetic measurements of macroscopic, room-temperature objects initially used a single-channel SQUID to map, for example, magnetic field distributions outside the human body or a sample of steel under uniaxial stress (13). Within the past several years, biomagnetic SQUID systems have evolved into complex arrays of as many as 250 SQUIDs optimized for measuring the magnetic field from electrical activity in the intact human brain. Magnetic imaging of smaller samples has evolved in an opposite direction into scanning SQUID microscopy, wherein a single-channel SQUID images the magnetic fields by means of a raster scan of the sample

relative to the SQUID. Many such instruments have been built, with pickup coil diameters ranging from 4 μm to 2 to 3 mm.

Scanning SQUIDs have been used to image the magnetic fields from a wide variety of sources, ranging from the developmental currents generated by the embryo in a chicken egg to the persistent currents associated with quantized flux in superconductors. The interested reader is referred to previous reviews for more details on the history of this microscope, on experimental considerations, and on applications to, for example, biology and biomedicine (13–18). In this review, we outline the most important features of SQUID microscopy, the design considerations that make SQUID microscopes well-suited for particular materials science applications, and discuss in detail several measurements of interest to the materials science community. We do not attempt to review the details of construction of the various instruments.

SQUID Magnetometers

When two superconductors are separated by a sufficiently thin insulating barrier, it is possible for a current to flow from one to the other, even with no voltage applied between them. In 1962 Josephson (19) predicted the existence of this supercurrent and calculated that it should be proportional to the sine of the quantum mechanical phase difference between the two superconductors. This dependence of the supercurrent on the relative phase difference, when combined with an intimate relationship between this phase and the magnetic field, is the key to a class of sensitive magnetic field detectors called SQUIDs (20–22). The type of SQUID used most commonly for microscopy, the dc SQUID, is composed of a superconducting ring interrupted by two such Josephson junctions. The maximum zero-voltage current (the critical current) of the dc SQUID varies sinusoidally with the integral of the magnetic field through the area of the SQUID loop owing to interference of the quantum phases of the two junctions. The period of modulation is the superconducting flux quantum $h/2e = 2.07 \times 10^{-15}\ \mathrm{T \cdot m^2}$. With flux modulation, phase-sensitive detection, and flux feedback (Figure 1) (23, 24), this phase can be measured to a few parts per million with a one-second time integration. This makes the SQUID the most sensitive sensor of magnetic fields known.

The overriding advantage of the SQUID microscope is its high field sensitivity. Magnetometer sensitivity can be specified in terms of the system noise in units of flux, energy, or field. Typically, the ultimate field sensitivity of the SQUID microscope is given by the SQUID flux noise divided by the effective pickup area. For typical values of flux noise of $2 \times 10^{-6}\Phi_0/\sqrt{\mathrm{Hz}}$, a pickup area of $(7\ \mu\mathrm{m})^2$ corresponds to an effective field noise of $\sim 1 \times 10^{-10}\ \mathrm{T}/\sqrt{\mathrm{Hz}}$, whereas a pickup area of $(1\ \mathrm{mm})^2$ corresponds to an effective field noise of $\sim 4 \times 10^{-15}\ \mathrm{T}/\sqrt{\mathrm{Hz}}$. For the larger pickup areas, various schemes, such as

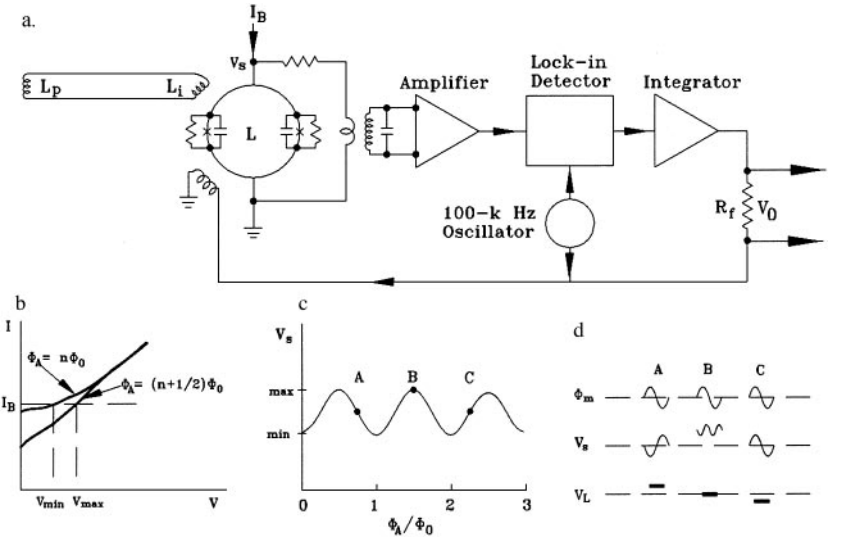

Figure 1 A dc SQUID. (*a*) A simplified circuit for a dc SQUID magnetometer. (*b*) The current-voltage characteristic of a SQUID without feedback with two different values of the flux threading the SQUID loop. The amount of applied flux, Φ_A, determines the voltage output, V_s, for a particular value of bias current, I_B. As the applied flux varies between $\Phi_A = n\Phi_0$ and $\Phi_A = (n+1/2)\Phi_0$, the output voltage changes between V_{min} and V_{max}. (*c*) The V-Φ curve of a dc SQUID, with constant bias current. (*d*) The voltage response of the SQUID to a modulating flux, Φ_m. The response varies greatly depending on the value of Φ_A. Three possible points are highlighted to illustrate the response of a SQUID and the feedback needed to lock the SQUID to operation at an extreme value. From top to bottom we see: one cycle of the flux modulation, Φ_m, applied to the SQUID operating at three different locations on the V-Φ curve, the voltage response of the SQUID, V_s, and the necessary feedback of the flux-locked loop, V_L, which applies a counter flux to the SQUID loop to return the system to an extreme position on the V-A curve (adapted from Reference 24).

gradiometric SQUIDs or SQUID pickup coils, multiple SQUIDs that form electronic gradiometers, magnetic shields, or active noise cancellation must be used to reduce the effects of environmental noise; the practical limit for sensitivity of several $\mathrm{fT}/\sqrt{\mathrm{Hz}}$ for $(1\ \mathrm{cm})^2$ SQUIDs is usually set by the combination of SQUID, shield, sample, and dewar noise (25). Nevertheless, the SQUID microscope is the most sensitive instrument for imaging magnetic fields with spatial resolutions larger than a few microns. Modeling indicates current sensitivities of $\sim$1 $\mathrm{nA}/\sqrt{\mathrm{Hz}}$ and spin sensitivities of $\sim$1000 μ_B for a 50 $\mu\mathrm{m}^2$ pickup area.

Other advantages for SQUID microscopes include the ability to detect with undiminished sensitivity small spatial changes in large magnetic fields, a bandwidth from dc to tens of kilohertz or higher, and a readily controlled geometry that allows the fabrication of differential magnetometers with a common mode

rejection of magnetic noise as great as 120 db. They have the disadvantages of relatively modest (tens of microns) spatial resolution and the requirement of a cooled sensor, which brings with it the large size of a dewar and the operational and technical complexity of cryogenics.

Scanning SQUID Microscopes

In this article, we consider a scanning SQUID microscope (SSM) as any scanning SQUID system with pickup coils of diameter several millimeters or fewer that is used to acquire images of a magnetic field. Much of the experience with SSMs that was gained at the millimeter scale, for example sample scanning, optimization of spatial resolution, and image deconvolution techniques, is directly applicable to the micron-sized pickup coils of the smallest systems.

There are numerous schemes for scanning the sample and for coupling the sample field into the SQUID sensor. These schemes can be conceptually divided into two classes (Figure 2). In the first (Figure 2*a–c*), both sample and SQUID are held at low temperatures either in a common vacuum space or in a cryogenic fluid. This allows for the minimum spacing between SQUID and sample and therefore for the best spatial resolution. If the SQUID and sample are in the same

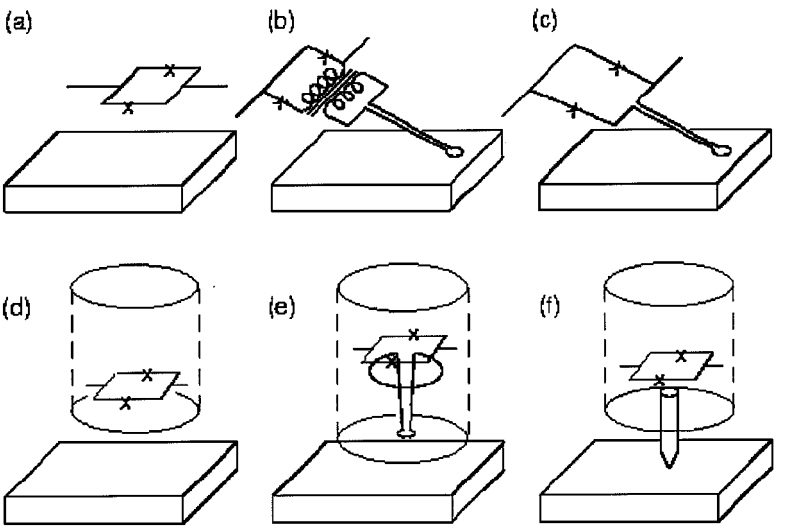

Figure 2 Various strategies have been used for scanning the sample relative to the SQUID. Both sample and SQUID sensor can be cooled (*a–c*) or only the SQUID (*d–f*). The field at the SQUID can be detected (*a*,*d*), or a superconducting pickup loop can be inductively coupled to the SQUID (*b*,*e*), or the pickup loop can be integrated into the SQUID design (*c*). In (*f*), a ferromagnetic tip is used to couple flux from a room temperature sample to a cooled SQUID.

vacuum, it is then possible to operate them at different temperatures, for example the SQUID can be held at 4.2 K while the sample is maintained at 100 K. In the second class (Figure 2*d–f*), the SQUID is cold but the sample is warm and can be exposed to the atmosphere. In this case the SQUID and sample are separated by some form of thermal insulation. This has the advantage of not requiring sample cooling, but entails some sacrifice in spatial resolution. In either case, a bare SQUID (panel *a*,*d*), a SQUID inductively coupled with a superconducting pickup loop (panel *b*,*e*), or a superconducting pickup loop integrated into the SQUID design (panel *c*), can be used to detect the sample magnetic field.

While early SQUID systems utilized discrete SQUID sensors connected to hand-wound wire pickup coils, the use of thin-film processing techniques to produce a SQUID sensor that is integrated with the pickup coil is now commonplace. The integrated design (see Figure 3) has two advantages: First, the pickup loop area can be made small, with well-shielded leads so that it is only sensitive to the local variations of the sample magnetic field, while at the same time providing optimal coupling of the pickup loop flux to the SQUID. Second, this geometry reduces the influence on the sample of both the SQUID self-fields and the flux modulation typically used in the feedback scheme of dc SQUIDs. However, close coupling between the ac electromagnetic field generated by the SQUID and the sample can be used to advantage, for example to image samples at very high frequencies (26–29).

While for the second class of SQUID microscopes it is possible to construct dewars such that a pickup coil immersed in liquid helium can be less than 2 mm from room temperature, separations smaller than that require placing the SQUID in the vacuum space between the cryogen reservoir and room temperature. The SQUID is then cooled by a high-thermal conductivity link of copper or sapphire or by cryogen flowing in a channel adjacent to the SQUID. The SQUID is separated from room temperature by a thin sapphire, silicon, or silicon-nitride window (17). With careful design, the spacing between the cooled SQUID and

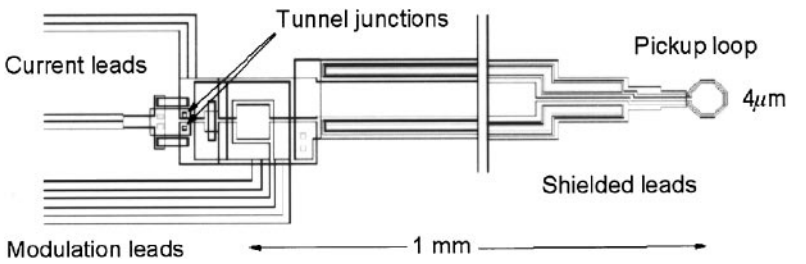

Figure 3 Schematic of a Nb-Al_2O_3-Nb trilayer integrated SQUID. The pickup loop is connected through well-shielded leads to the body of the SQUID.

the warm sample has been made as small as 15 μm (30–32) for high-temperature superconductivity (HTS) SQUIDs and 100 μm (33) for low-temperature superconductivity (LTS) ones. The key point for high resolution SQUID magnetometers is that there is essentially no heat conduction through the vacuum, and only a small aperture is required in the thermal shields that surround the SQUIDs and/or its pickup coils. Hence, the radiative load from room temperature to even a helium-temperature SQUID is typically only a few milliwatts.

It was recently proposed (Figure 2*f*) that magnetic flux can be coupled from the sample into the SQUID using a sharp ferromagnetic tip (34, 35). This technique has the advantage that the SQUID is thermally isolated from the sample, while at the same time sensing the flux from only a submicron area of the sample. Some disadvantages of this scheme are that the efficiency of flux coupling is relatively low, the coupling material may introduce nonlinearities and magnetic noise, and all components of the magnetic field are sensed, to date, in a manner that is poorly understood.

Several of the microscope systems that have been built can provide a perspective as to the absolute capabilities of the technique. Ten years ago, the resolution limit for room temperature samples was achieved with a four-channel SQUID whose 3-mm diameter pickup coils are 1.5 mm from room temperature and have a noise of 100 fT/$\sqrt{\text{Hz}}$ (36). Within the last five years, the great advance in resolution was achieved by the Maryland group, which developed an HTS SSM that is 40 μm from a room temperature sample (16), provides 50-μm spatial resolution, but has 34 pT/$\sqrt{\text{Hz}}$ noise at 100 Hz and 260 pT/$\sqrt{\text{Hz}}$ at 1 Hz (bias switching should improve the low-frequency performance); a commercial version of this instrument provides a sensitivity of 20 pT/$\sqrt{\text{Hz}}$, an unenhanced spatial resolution of 50 μm, and the ability to detect for a wire 100 μm from the SQUID currents as low as 10 nA with a 1-s averaging time (37). Lee et al have fabricated an inverted HTS system designed for biological measurements (31, 32) that uses a 3-μm thick silicon nitride window so that the separation between the 40 μm SQUID and the room-temperature sample is as low as 15 μm.

The capabilities of systems with cryogenic samples is even more impressive. SQUID microscopes have been demonstrated with a spatial resolution as fine as 4 μm for samples that are in the same cryogenic environment as the SQUID sensor (14, 16, 38–44). Systems with both the sample and the SQUID immersed in liquid helium have 66 μm resolution and 5.2 pT/$\sqrt{\text{Hz}}$ noise at 6 kHz (42), and 10 μm at 100 pT/$\sqrt{\text{Hz}}$ (43); the Conductus Scanning Magnetic Microscope™ provided micron resolution for helium-temperature samples (38). The first- and second-generation IBM low-transition-temperature (LTS) SQUID microscopes (44, 45) have octagonal pickup coils as small as 10 and 4 μm in diameter, respectively, and can map single magnetic flux quanta, ϕ_0, trapped in superconducting films, with a system noise of less than 2 $\mu\phi_0/\sqrt{\text{Hz}}$ or 40 pT/$\sqrt{\text{Hz}}$. Wellstood

et al built liquid nitrogen systems with a $(10\ \text{mm})^2$ field of view, 80 μm spatial resolution, 80 pT/$\sqrt{\text{Hz}}$ noise at 1 Hz (39) and 25 pT/$\sqrt{\text{Hz}}$ above 500 Hz, and one SSM with 15 μm resolution (40).

Although LTS SQUIDs are more robust and sensitive, there is an appeal in using HTS SQUIDs due to a more modest refrigeration requirement that could be readily met by a commercial, closed-cycle refrigerator. For samples at low temperatures or in vacuum, LTS niobium SQUIDs offer the greatest sensitivity at little inconvenience. Until recently the choice of high- or low-temperature SQUIDs for imaging exposed samples at room temperature had been determined by the tradeoff between resolution and sensitivity. Measurements requiring high sensitivity, particularly at low frequencies, have utilized LTS SQUIDs, but with a spatial resolution limited to about 1 mm. Measurements requiring a resolution of tens of microns have utilized HTS microscopes, despite their higher noise, especially at frequencies below 10 Hz. The demonstration that LTS SQUID can be operated within 100 μm of a room temperature sample (33) will now extend the sensitivity of SQUID microscopes by at least an order of magnitude.

Given this introduction, we now proceed to discuss several key aspects in the design and implementation of these instruments.

Scanning

Because of the sensitivity of the SQUID to rotation in an external magnetic field or translation in an external field gradient, the SQUID is typically held stationary and the sample is moved. Scanning of the sample relative to the SQUID has been accomplished in a number of ways. Although piezoelectric scanning has been used for SQUID microscopy (46), the scan range available from piezo drives is generally too small (typically a few microns at low temperatures) to be useful. We should note, however, that a new type of cryogenic piezoelectric scanner used in scanning Hall bar systems has achieved low-temperature scan ranges of over 100 μm (47) and may prove useful for an SSM. Most systems with cooled samples use push rods or levers to transfer the mechanical motion from room-temperature motors, although cryogenic motors are feasible (38). Microscopes with warm samples use Inchworm$^{\text{TM}}$ piezoelectric motors or more conventional servo or dc motor-driven scanning systems, although care must be taken to avoid generating spurious magnetic signals with the scanning system. As with any raster-scanned imaging technique, the speed with which the sample is scanned is the rate-limiting step in image acquisition: Given the kilohertz bandwidth of the SQUID, scan time is often limited by motor speed rather than by the response time of the SQUID, and for macroscopic samples, linear velocities of 10 cm/s allow a 10 cm $\times$ 10 cm sample to be imaged with millimeter resolution in 2 min. High scan speeds can also shift the measurement bandwidth away from the low-frequency noise that plagues HTS SQUIDs; for a given total

scan time, the average of multiple high speed scans may exhibit lower noise than would a single slower scan acquired in a narrower, but noisier, frequency band.

Spatial Resolution

Quantitative analyses of magnetic imaging (17, 48–55) have shown that a SQUID will have the best combination of spatial resolution and field sensitivity if the pickup-coil diameter is approximately the same as the spacing between the pickup coil and the sample; similar arguments will apply to other point-detection means of measuring the magnetic field. Thus a high-resolution instrument requires a small pickup coil to be placed close to the sample. Because SQUID microscopes usually have only a single SQUID, the separation between scan lines must equal the desired spatial resolution, which is comparable to the coil diameter. It is important to recognize that the separation of features in a magnetic image can be enhanced with image processing that utilizes a priori knowledge of the geometry and thus the transfer function between the source of the magnetic field and the SQUID. In this context, imaging algorithms can be viewed as inverse spatial filters and hence subject to noise-induced instabilities due to the amplification of high spatial frequencies that had been preferentially attenuated with distance from the source. Although it is possible to design multi-turn pickup coils that are corrected for the blurring effects of finite coil size and coil-to-sample separation, i.e. are apodized (56), such SQUIDs have yet to be fabricated. The application of inverse imaging techniques to magnetic imaging is reviewed in detail elsewhere (57) and has been shown to be useful in commercial instruments (37).

Sensitivity

The obvious goal would be to make SQUID microscopes ever-closer to the sources with ever-finer spatial resolution, but there is a corresponding loss in sensitivity to magnetic field as the SQUID is miniaturized. However, the performance enhancements achieved by miniaturization of SQUID microscopes are governed not only by the sensitivity of the SQUID sensor, but also by the rate of fall-off of the field produced by the elements of a distributed source. The coupling of these factors can be examined by specifying sensitivity in terms of a noise-equivalent source defined as the minimum detectable source in a unit bandwidth, e.g. the minimum detectable current in a wire, $I_{\min}$; the minimum detectable current dipole, $p_{\min}$, in a conducting medium; or the minimum detectable magnetic dipole, $m_{\min}$. The advantage of this approach is that it is possible to compare widely different magnetometer configurations, both before and after image reconstruction, in terms of the sources that are being sought. It is functionally equivalent to referring an amplifier noise to the input; in this

case the input to the SQUID is not the magnetic field, but rather the source that produces it.

Following the treatment by Wikswo (17), we assume that the SQUID has a certain energy sensitivity, that the flux sensitivity can be adjusted by changing the junction and washer geometries, and that the volume sensed by the pickup coil (proportional to the cube of the linear coil dimension, a) contains a fixed field energy density optimally coupled to the SQUID by the correct choice of the numbers of turns in the pickup coil. From these assumptions, we see that the smaller the magnetometer, the lower its absolute field sensitivity, but because smaller magnetometers can be placed closer to the sample, there is an increase in the field produced by the source.

If the source is a wire a distance a from the SQUID pickup coil, also of dimension a, the magnetic field strength is proportional to $1/a$. As the magnetometer is made smaller and closer, the field strength increases as $1/a$, and the SQUID sensitivity decreases as $a^{3/2}$, so that the minimum current detectable by the magnetometer is proportional to $a^{-1/2}$, i.e. a smaller, closer magnetometer cannot detect as weak a current in a wire as can a larger, more distant magnetometer. If the sole object of an experiment is to detect the presence of a current-carrying wire, little is gained by miniaturizing the magnetometer, since the larger, more distant magnetometer is able to detect weaker currents, and design compromises during the miniaturization process may lead to further reductions in sensitivity. If the objective is to localize the current-carrying wire and discriminate one wire from another, then miniaturization will help as long as the wires can carry adequate current to provide the requisite signal-to-noise ratio.

If the magnetic field source is a magnetic flux quantum trapped in a vortex in a superconducting sheet or a current dipole immersed in a conducting medium, typical of a corrosion or bioelectric system, the magnetic field is proportional to $1/a^2$, so that the minimal detectable source is proportional to $a^{1/2}$. There is a slight increase in detectability with smaller, closer magnetometers, assuming that the SQUID energy sensitivity is independent of a.

The case for magnetometer miniaturization is stronger for magnetic fields that are produced by magnetic dipoles. Since the magnetic field scales as $1/r^3$, while the sensitivity scales as $a^{3/2}$, the minimum detectable magnetic dipole, $m_{\min}$, goes as $a^{3/2}$. Small a means that $m_{\min}$ is small and hence good. This is why the relatively insensitive magnetometer used in a magnetic tape recorder or a disk drive can give very large signals: the spacing between the magnetic dipoles and a tape head can be on the order of 1 μm or less. Similarly, the magnetic force microscope is an intrinsically insensitive magnetometer, but for imaging the strong magnetic dipoles written on a computer disk, it can obtain a spatial resolution on the order of 10 nm with tip-to-surface spacings of 1 nm. However, the field sensitivity of this type of device is five orders of magnitude

worse than what can be achieved with a SQUID microscope (43). Thus the optimization of a SQUID microscope is governed not only by the nature of the source, but also by the intended measurement. For some measurements, SQUIDs are ideal.

APPLICATIONS

The majority of the effort in SQUID microscopy appears to have been directed toward the development of the instruments and the demonstration of the technique, particularly for biomagnetism, corrosion science, and non-destructive evaluation (NDE). The use of SSMs in biomagnetism is reviewed elsewhere (17) and is not addressed here. Instead we review briefly the applications to NDE and corrosion and concentrate most of our attention to measurements on superconductors, where SQUID microscopes have made the most significant scientific contributions.

Non-Destructive Testing

Because of their ability to measure magnetic fields under a variety of conditions, SQUIDs can be used in a number of different NDE modes (58). The easiest SQUID NDE measurements involve intrinsic currents, for example in a printed or integrated circuit, as is shown in Figure 4*a*. Remanent magnetization, perturbations in applied currents, or Johnson noise in metals can be detected, as shown in Figure 4*b–d*. With the application of an ac field, SQUIDs can image eddy currents (Figure 4*e*); the hysteretic magnetization in steel can be examined if cyclic stress or coincident ac and dc magnetic fields are applied, as shown in Figure 4*f*. In a dc magnetic field, as in Figure 4*g*, SQUIDs can be used to image the magnetization of diamagnetic and paramagnetic materials, including superconductors. Each of these applications is reviewed in detail elsewhere (18), so that we need only review several measurements that may have potential utility to materials science.

Because SQUID magnetometers can achieve their full sensitivity in the presence of strong applied magnetic fields, they are well suited for imaging of plastics and other materials that are generally considered nonmagnetic, but in fact have a measurable diamagnetic susceptibility. Two- and three-dimensional magnetic susceptibility imaging offers potential advantages for imaging composites with dilute magnetic tracers and for magnetic imaging of materials such as plastic, titanium, or aluminum. One example of this approach involved the mapping of the remanent magnetization and magnetic susceptibility of a 50-μm slice of volcanic rock to allow identification of the matrix component responsible for various aspects of the magnetic properties of the bulk composite (59). As LTS and HTS SQUID microscopes become more widely recognized, studies

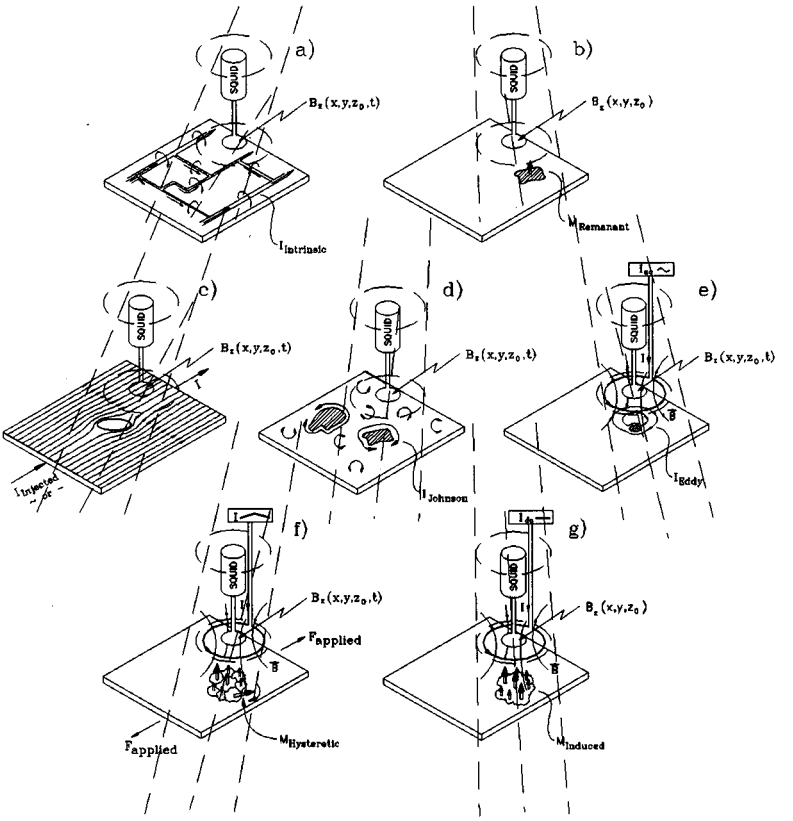

Figure 4 The modes of SQUID NDE. By scanning the sample beneath the SQUID, it is possible to image (*a*) intrinsic currents, (*b*) remanent magnetization, (*c*) flaw-induced perturbations in applied currents, (*d*) Johnson noise in conductors, (*e*) eddy currents and their perturbations by flaws, (*f*) hysteretic magnetization in ferromagnetic materials in the presence of an applied stress, and (*g*) diamagnetic and paramagnetic materials in an applied field (from Reference 58, with permission).

such as these should become much more common. Similarly, these microscopes may prove useful for studies of the microscopic magnetic behavior of ferromagnetic materials, as has been shown on a larger scale by Weinstock et al (60).

Much of the work on SQUIDs for NDE has not emphasized spatial resolution because the capability of greatest interest is the sensitivity that allows the detection of perturbations in extremely low-frequency eddy currents associated with flaws deep inside a conductor such as aluminum: Signals originating a millimeter or more within a sample require only a comparable spatial resolution. A technique that has undergone extensive development for aircraft NDE

is the use of a sheet conductor carrying an alternating current to induce planar eddy currents in the test sample (61). Application of currents from two orthogonal directions and the use of phase-sensitive detection and analysis techniques allow the SQUID to be used for depth-selective, oriented eddy current imaging that can distinguish the signature of a subsurface crack from the larger signal from an adjacent rivet. For many NDE applications, the signal strength is determined by an applied field or current, and hence the signal-to-noise ratio of the image would be limited not by SQUID noise but by spatial variations in the material properties or structure of the sample (62), suggesting the possible utility of this approach for mapping subsurface heterogeneities in metals (63). The suitability of high-resolution SSMs to eddy current measurements has already been demonstrated (26, 64), thus their extension to this area of study should be straightforward. One possible limitation of miniaturizing instruments that utilize an applied ac or dc magnetic field is the need to shield the SQUID sensor itself from a strong magnetic field that would normally be applied to a sample and to the adjacent gradiometric or differential pickup coil but not the SQUID itself; gradiometric SQUIDs can reduce this problem but not eliminate it.

As a first demonstration of the capabilities of a SQUID to detect imperfections in wire stock prior to it being drawn into a fine wire, Weinstock (65) has used scanning SQUIDs to image the field perturbation associated with a 300-μm hole drilled partway into 500 μm diameter copper and aluminum wires carrying 16 mA at a kilohertz. A similar approach was used in composite superconducting wires to detect at room temperature the magnetic field fluctuations that are associated with conductivity anomalies related to sausage-like discontinuities in individual strands of the conductor. The sensitivity of the technique is limited by the linearity of the wire. Superconducting wire is sufficiently stiff that this approach can be readily applicable to quality control during manufacture or acceptance-testing of composite superconducting wire, although it may be somewhat more difficult to utilize in the soft-wire industry. There could be significant financial or practical benefits from finding flaws in wire stock before drawing it to a finer gauge or in stranded superconductor wire prior to the winding of expensive magnets.

Because of the straightforward and unique relation between the current distribution in a planar sample and the magnetic field adjacent to that plane (57), the SSM is ideally suited for mapping currents that cannot be imaged by other means. One of the most promising practical applications for SSM current imaging involved detecting short circuits in electronic integrated circuits and multichip modules (MCM). For example, in CMOS circuitry, a short involving a power bus could inactivate large regions of a circuit and prevent the device from receiving adequate voltage or functioning sufficiently well to allow more conventional diagnostic tests that would localize the region containing the short:

For example, the detection of secondary electrons in a scanning electron microscope can be used to observe the voltage of individual gates as they switch, but on only the top layer of metalization of an exposed silicon chip, and typically only when the gates can operate over the normal range of voltages. Thermal imaging is limited by the thermal conductivities of the silicon substrate and the thermal diffusivity of the surrounding package. Neocera (37) has recently introduced a commercial SSM that can non-destructively detect package-level shorts through the device packaging and multiple metalization layers. Figure 5 shows examples of images of a faulty MCM and demonstrates the capabilities of both cryocooled HTS SSM and image deconvolution techniques for this application. As the technology matures, there will undoubtedly be additional, commercially viable applications of SSMs.

Corrosion

Scanning SQUID microscopes are currently being evaluated for laboratory studies of hidden corrosion in aircraft lap joints and may well have a much wider applicability to corrosion science. The potential for this area of research and the relationship of the SQUID technique to other more common ones was outlined by Wikswo (66): Quantitative measurement of corrosion activity on exposed metal surfaces is possible with conventional voltammetry, using a potentiostat, and with electrochemical impedance spectroscopy (EIS), a rapidly developing research technique that allows the study of corrosion reactions in low-conductivity media where meaningful measurements with a DC potentiostat are difficult. EIS has also been used to evaluate organic coatings. Scanning potentiostats, including ones based on a vibrating probe technology developed for measuring steady biological electrical currents, can be used to obtain corrosion current distributions in the vicinity of individual corrosion pits. However, while these analytical techniques are useful for exposed metal surfaces, they are of little utility for studying in situ hidden corrosion in crevice corrosion, corrosion in aircraft lap joints, or corrosion beneath thick layers of paint or specialized coatings. Despite the military and commercial importance of corrosion of aircraft aluminum, there are no established techniques for determining the instantaneous corrosion rates in, for example, an aircraft lap joint. As a result, studies of these phenomena typically require the creation of redundant samples that are examined destructively at regular intervals throughout the duration of test; the measurement interval is typically a year: Instantaneous rates and how they are affected by the environment are unknown. The test cycles are frequently shortened by use of exposure protocols that accelerate corrosion, but it is unclear whether accelerated corrosion adequately represents actual corrosion; while the rate of accelerated corrosion can be measured by morphological

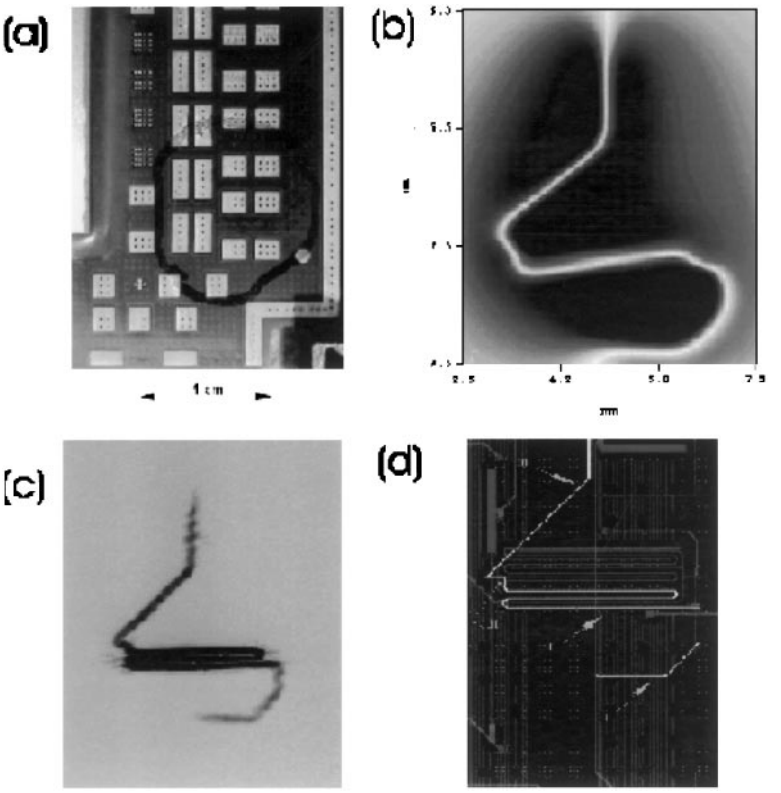

Figure 5 SQUID imaging of integrated circuits obtained by a cryocooled HTS SSM with a working distance of 340 μm between the SQUID and the multilayer circuits within the intact, room temperature package (37). (*a*) An optical photograph of a multichip module (MCM) package. The *hand-drawn circle* indicates the region where a short was localized with thermography. (*b*) The raw magnetic image obtained from a scan of the component of the magnetic field perpendicular to the area of the sample in (*a*). The *wide white line* corresponds to the region of zero field in the z direction, which to a first approximation corresponds to the path of localized current; the magnetic field is of opposite sign on either side of this line. (*c*) The image of the current found from this field inverse spatial filtering. The spatial resolution measured across the serpentine of current has a full-width at half-maximum of 75 μm or ± 38 μm. (*d*) Comparison of the data obtained from the SSM when overlaid with the circuit drawings allowed the circuit fault to be located with an accuracy of better than ± 40 μm. The computed current path is shown in *white* on top of the background metalization. Courtesy of Neocera, Inc.

analysis, it is difficult if not impossible to extrapolate the rates from accelerated studies to those for realistic environments.

Because of its unparalleled sensitivity (up to 5 fT/$\sqrt{\text{Hz}}$), spatial resolution (microns to millimeters, depending upon the desired sensitivity), and dc-to-10 kHz bandwidth, the SSM is unequaled in its ability to image the temporal and spatial variation of the magnetic field associated with ongoing, hidden corrosion in aluminum lap joints or other complex structures. In terms of basic studies on corrosion, the SSM should be ideal because it can be used to map steady or time-varying currents deep within a sample without having to make contact with the sample or expose the metal that is undergoing corrosion for visualization or measurement. Relative to the sensitivity of a SQUID, a very strong electric current is required to dissolve any macroscopic amount of metal: Approximately 300 coulombs of charge are required to corrode away a 0.1-mm thick layer of aluminum from a 1 cm^2 sample, which would correspond to a current of 160 nA flowing for 80 years. As discussed above, the limit of sensitivity of an SSM approaches a nanoamp. Because an SSM can be used to image a current distribution within a lap joint or in the metal beneath a thick coating without disturbing the sample, it can be used to monitor the spatiotemporal distribution of ongoing corrosion activity in real time.

Despite the potential of SQUIDs for research into the prevention of corrosion of aircraft aluminum, there have been only limited published studies regarding the application of SQUIDs to corrosion research. Several years ago, a group at MIT demonstrated that SQUIDs could be used to measure corrosion noise in a zinc sample immersed in concentrated hydrochloric acid (67–70), but these studies effectively utilized the SQUID as a low-impedance, low-noise ammeter incorporated into a conventional electrochemical measurement system and did not, in fact, explore the ability of SQUIDs to make measurements that would otherwise be impossible with conventional techniques. Hibbs et al have shown that SQUIDs can detect filiform corrosion underneath the paint covering aircraft aluminum and can map the corrosion in a simulated lap joint exposed to concentrated sodium hydroxide and have pointed out that the observed magnetic fields were significantly smaller than would be expected from Faradaic considerations alone (71–73). Recently, a German group has shown that a high-temperature superconductivity SQUID can be used to detect corrosion in aluminum aircraft components (74). The Vanderbilt group has conducted a number of studies that have defined the capabilities of the SSM for quantitative measurements of corrosion (66, 75–78). They have shown that an SSM can image the temporal and spatial variation of corrosion in aircraft aluminum, distinguish between the time course of corrosion in 2024 and 7075 aluminum, detect crevice and stress-corrosion cracking, detect corrosion of aluminum in salt solutions as dilute as one part per million NaCl, and map the distribution of

corrosion activity from the opposite side of aluminum samples as thick as one centimeter.

There are, however, several issues in magnetic measurement of corrosion currents that need to be resolved and are the subject of ongoing research at Vanderbilt. Let us consider a simple, idealized corrosion system involving an aluminum plate that forms the upper surface of a half space filled with an electrolyte solution. The electromotive forces that are associated with the corrosion activity and that drive the currents detected magnetically by the SSM above the plate can be modeled as an infinitesimally thin electrochemical layer at the interface between the aluminum and the electrolyte. If the electrolyte and aluminum are both electrically isotropic, it follows from symmetry arguments that there is no magnetic field in the half space above the aluminum. The experimental observation of corrosion-related magnetic fields outside an aluminum-electrolyte system indicates that this simple model is wrong: Intergranular corrosion, intergranular conductivity differences, anisotropies from rolling, and the effects of sample boundaries can break the symmetry of the simple model and lead to measurable magnetic fields, albeit an order of magnitude (or more) smaller than those predicted by a back-of-the-envelope Faradaic consideration. The relative contributions of each of these factors may depend on the type of corrosion, e.g. pitting or uniform corrosion, and upon the microstructural properties of the metal and must be understood before it will be possible to realize the full potential for the SSM to study hidden corrosion. Elucidation of these factors may in turn provide a new perspective on the role of mesoscopic properties of materials in the corrosion process.

Thus the preliminary work using SQUIDs to monitor currents from either exposed or hidden corrosion demonstrates that SQUIDs are well suited for the periodic, non-destructive analysis of corrosion test specimens where the corrosion activity is not directly accessible to a potentiostat, e.g. corrosion that is hidden under a thick coating or one or more layers of metal. In fact, while numerous techniques (such as X rays, ultrasound, thermal-wave, visual, and eddy-current measurements) can detect the accumulated metal loss associated with long-term corrosion, SQUIDs may be the only instrument that can detect the instantaneous hidden corrosion currents non-destructively. However, before the full capability of SQUID magnetometers can be utilized for obtaining the rates, it is necessary to establish from fundamental principles the factors governing the relationship between corrosion currents and their magnetic fields.

Superconductivity: Quantized Flux and Vortex Trapping

Because the sample must be kept cold in the highest spatial resolution SSMs, it is natural to use them to study superconducting systems. In fact, some of the most exciting applications of the SSM have arisen from such studies. We begin

with a brief review of earlier studies of quantized magnetic flux with a scanning SQUID and then examine in detail current applications of the technique.

When a hollow superconducting cylinder in a magnetic field is cooled through its superconducting critical temperature, T_c, while in a magnetic field, the magnetic flux that remains inside the cylinder is quantized, consistent with London's prediction (79). The first demonstration of flux quantization was made by Deaver & Fairbank (80) and independently by Doll & Näbauer (81), using non-superconducting magnetometers with low spatial resolution. Similarly, when a type II or thin film superconductor is cooled through T_c in a magnetic field, some of the magnetic field is excluded (the Meissner effect), but some of it is trapped in quantized units called superconducting vortices. Each vortex has $\Phi_0 = h/2e$ (the superconducting flux quantum) units of magnetic flux surrounded by a persistent current flowing in the adjacent superconductor. Immediately after the invention of the SQUID magnetometer, Zimmerman & Mercereau (82) provided the first direct confirmation of the presence of individual quantized vortices pinned in a niobium wire by scanning a 50 μm diameter wire through a window in a two-contact SQUID (20, 21). By observing the shift in the critical current pattern as the wire was moved through the SQUID at a rate of 2 mm/min, they were able to image trapped flux with a spatial resolution of 200 μm, as shown in Figure 6. The SQUID was made by bending a wire over a ribbon, leaving a small window. This represents the first published image from a SQUID microscope, albeit a one-dimensional one.

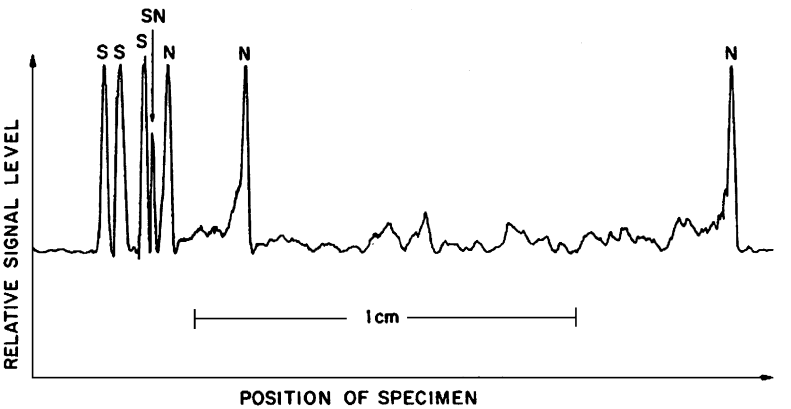

Figure 6 The first SQUID image of trapped flux in a 50 μm diameter niobium wire. The wire was pulled through a two-junction SQUID. *S* and *N* indicate the direction of the emerging field (from Reference 82, with permission).

The next SQUID microscope, also one-dimensional, was used to explain a perplexing feature observed in flux quantization measurements (83, 84). While the presence of flux quantization was clear in the early measurements on hollow cylinders, experiments that measured the average of many trappings, or even measurements on individual trappings, showed a continuous variation of the total flux with applied field, as shown in Figure 7*a*. For most values of the magnetic field applied to the cylinder before cooling it below T_c, the entire cylinder once cooled was found to be in the same quantum state with $\Phi = n\Phi_0 \pm 1\%$. However, for some initial applied fields, the cylinder appeared to be in a mixed state with bands along the length of the cylinder in states differing by one flux quantum (85). Figure 7*b* shows the SQUID microscope devised by Goodman & Deaver, in which a toroidal, single-point-contact RF SQUID was inductively coupled to a small pickup coil that surrounded a tin cylinder (14–56 μm diameter and 1000–5000 Å thickness) that could be scanned vertically. Figure 7*c* shows the resulting maps of the axial dependence of the flux trapped along the cylinder for different magnetizing fields. Integration of each of these maps to obtain the average flux threading the cylinder would exhibit the same continuous variation in trapped flux observed by the low-resolution SQUID that recorded Figure 7*a*.

The ability of a two-dimensional SSM to observe flux trapped in holes in a superconducting thin film was first demonstrated by Rogers & Bermon, who used a rudimentary SQUID/scanner system to image flux trapped in a thin niobium film with an array of 0.1 mm square holes that served as flux-trapping sites (86).

More recently, a particularly powerful application of SQUID microscopy has evolved in the detailed study of superconducting magnetic vortices trapped in planar superconducting films. With modern low-temperature SQUIDs and flux-locked loop electronics, flux noises of $\sim 1\mu\ \Phi_0/\sqrt{\text{Hz}}$ are attained. If the SQUID pickup loop is within a loop diameter of the sample surface, a large fraction (typically 50%) of the magnetic flux from a particular vortex can be intercepted by the loop. With a scanning rate of 0.1 s/pixel, this means that SQUID microscopes can image superconducting vortices with electronic signal-to-noise ratios of about 10^5. No other technique has this sensitivity.

One of the obstacles to the rapid development of superconducting digital circuitry has been interference from flux trapping. It is extremely difficult to cool superconducting chips without having some flux trapped in them. One strategy is to design holes in the superconducting ground plane to attract and trap flux in sections where it will do the least harm. An SSM is very useful to image the positions of trapped vortices and test the relative effectiveness of various flux trapping strategies. In fact, the first IBM SSM was built for this purpose (86). Figure 8 shows some results from a study of the relative effectiveness

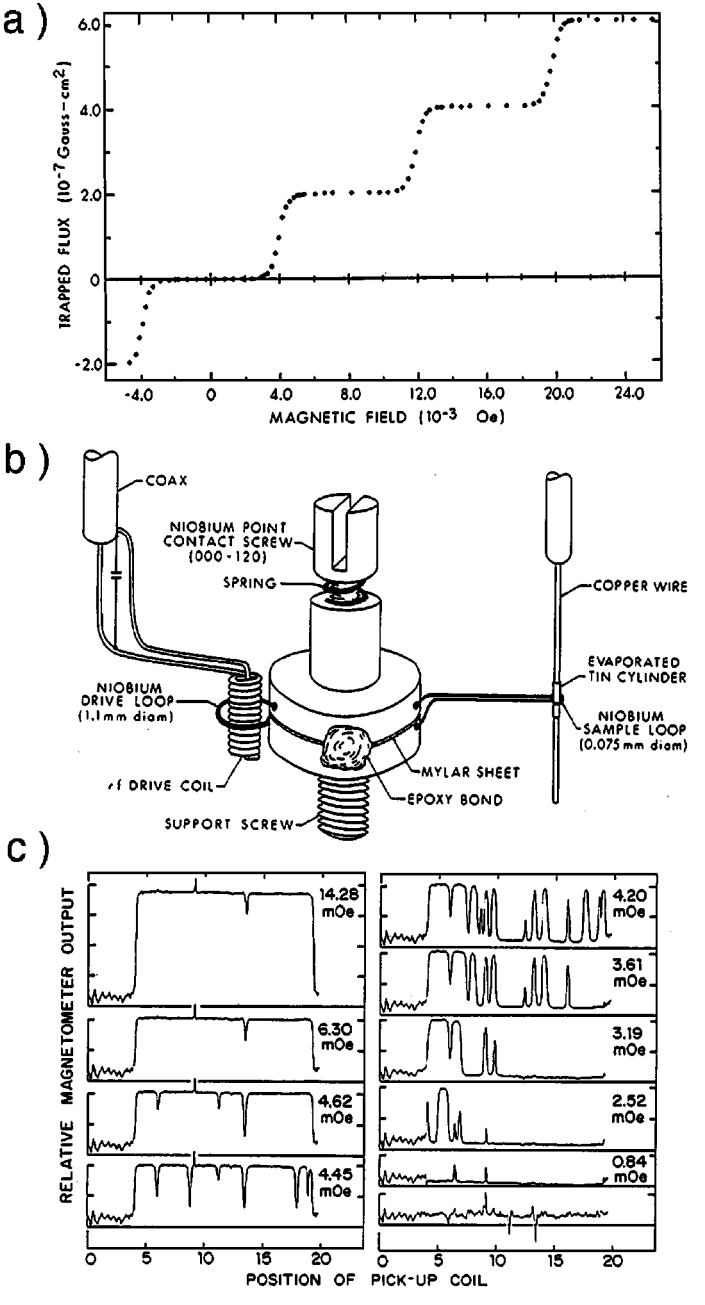
a)
TRAPPED FLUX (10^{-7} Gauss-cm^2)
6.0
4.0
2.0
0
-2.0
-4.0
0
4.0
8.0
12.0
16.0
20.0
24.0
MAGNETIC FIELD (10^{-3} Oe)
b)
COAX
NIOBIUM POINT CONTACT SCREW (000-120)
SPRING
COPPER WIRE
EVAPORATED TIN CYLINDER
NIOBIUM DRIVE LOOP (1.1mm diam)
NIOBIUM SAMPLE LOOP (0.075mm diam)
rf DRIVE COIL
MYLAR SHEET
EPOXY BOND
SUPPORT SCREW
c)
RELATIVE MAGNETOMETER OUTPUT
14.28 mOe
6.30 mOe
4.62 mOe
4.45 mOe
4.20 mOe
3.61 mOe
3.19 mOe
2.52 mOe
0.84 mOe
0
5
10
15
20
POSITION OF PICK-UP COIL

of two flux trapping schemes—small holes versus continuous moats (45). The SQUID image on the *left* (Figure 8*a*) shows a circuit with two rectangular patterns of 3×10 μm holes. The superconducting circuitry to be protected by these holes is within the rectangles. The sample was cooled and imaged in a field of 4 mG. The black dots in this image are vortices. Also seen are identification marks at the corners of the image, which are larger holes in the ground plane filled with magnetic flux. Note that even in this relatively modest field (the earth's magnetic field is about 100 times larger) two vortices are trapped in the region intended to be protected by the holes in the groundplane. The image on the *right* (Figure 8*b*) is of an identical circuit, but with two 3 μm wide rectangular continuous moats surrounding the superconducting circuitry. In this case, the sample was cooled in a field of 6 mG, and there are no vortices trapped in the sensitive region. Such studies indicate that it should be possible to design moat ground-plane structures to minimize the effects of flux trapping on superconducting digital circuits.

Superconductivity: Meissner Imaging

The initial stages of exploring novel superconducting compositions typically result in samples with small concentrations of superconducting material. It is therefore useful to image the samples in a way that determines which parts are superconducting. The SSM is an ideal tool for this.

Figure 9 shows an example of such a study (87). The *left* image in this figure is an optical micrograph of a sample made by processing a diffusion couple of $Sr_2CuO_3 + 0.05KClO_3$ in a gold capsule at 60 kbar and 950°C for 3 h. Bulk magnetization studies of the sample showed that the volume fraction of superconducting material was less than 3%. The *right* image in Figure 9 is a SQUID microscope image of the same sample, taken in a small ac magnetic field. The area showing "high" in this figure is where the ac field is sharply attenuated

←

Figure 7 SQUID measurements of trapped flux in cylindrical tin films. (*a*) The results of a low-resolution measurement on an entire cylinder that show the net trapped flux as a function of the magnetic field in which the cylinder was cooled below its transition temperature. These data were taken with a 24-mm long tin cylinder 56 μm in diameter and with walls about 500 nm thick. Note that the trapped flux can have a value intermediate between those expected by flux quantization. (*b*) The one-dimensional scanning SQUID magnetometer used for high-resolution measurements of the flux as a function of position along the cylinder. (*c*) The flux trapped in a small superconducting cylinder as a function of position along the length of the cylinder, demonstrating that different portions of the cylinder can be in different flux states and support differing persistent currents. The curves are labeled with the values of applied field in which the cylinder was cooled through its transition temperature. The bottom trace shows randomly distributed impurities in the Sn cylinder plus copper core with $T > T_c$ (adapted from Reference 84, with permission).

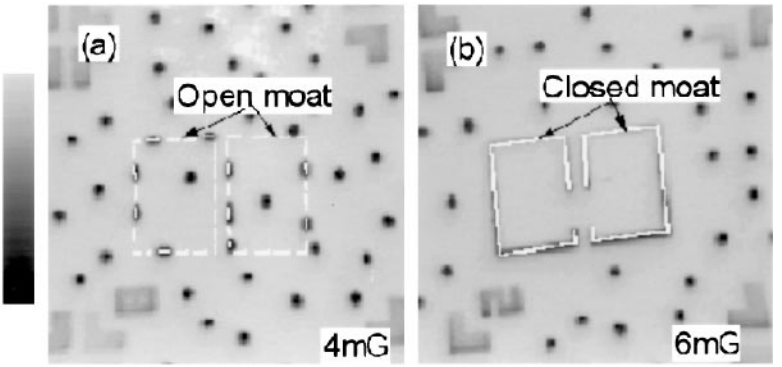

Figure 8 SSM study of the effectiveness of various flux trapping schemes. In this figure the layout of holes in the superconducting ground plane is indicated by *white lines* on top of the SQUID magnetic image. The *black dots* are superconducting vortices. In both cases the holes are intended to trap residual magnetic flux at locations away from the superconducting circuitry. In (*a*), the sample with 3×10 μm holes, with 10 μm spacing, has two vortices trapped in the superconducting circuitry when cooled in a field of 4 mG. In (*b*), cooled in 6 mG, a continuous moat keeps flux from trapping in the sensitive area (adapted from Reference 45).

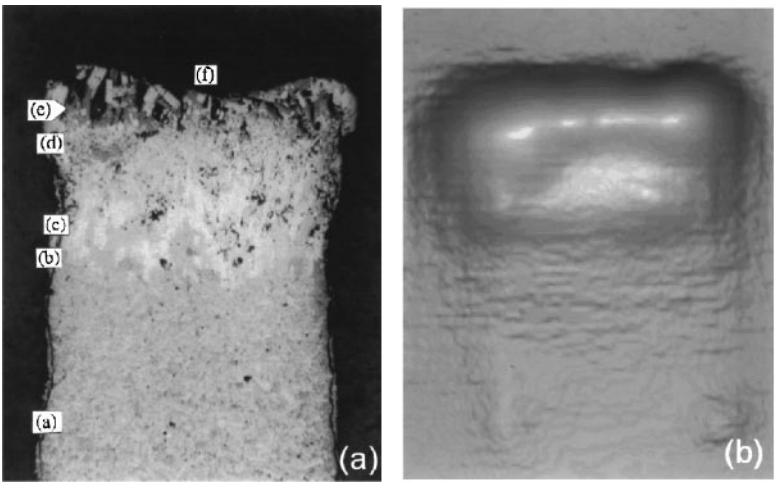

Figure 9 Optical micrograph (*a*) and SSM image (*b*) of identical fields of view of a superconducting sample made by diffusion between two components, processed at high temperatures and pressures. The bright areas in the SQUID microscope image are regions that show significant shielding of a small applied ac field and are therefore superconducting at low temperatures. Electron microprobe studies showed that the superconducting regions were composed of $Sr_3Cr_2O_5Cl$. This technique can detect superconducting concentrations below 1 ppm and represents a powerful way to search for unconventional superconductors. Reprinted by permission from *Nature* (Reference 87), copyright 1997 MacMillan Mag. Ltd.

above the superconducting portion of the sample due to Meissner shielding. The local Meissner shielding signal is nearly complete in some regions; these portions of the sample are completely superconducting. Measurements of the composition of these regions with electron-microprobe indicates that the superconducting material (the *dark grey* areas labeled *e* in Figure 9*a*) is $Sr_3Cu_2O_5Cl$. This scanning SQUID petrology technique should prove a valuable technique for rapidly identifying new superconducting compounds.

Meissner imaging can also prove useful for identifying problems in the processing of superconducting circuitry (Figure 10) (M Bhushan, JR Kirtley, MB Ketchen, unpublished data). Figure 10*a* is the schematic of a multilevel Nb superconducting test circuit with SiO_2 insulation. This test circuit was exposed to a radio-frequency plasma sputter cleaning step. Although transport measurements show no reduction of conductivity at room temperature, there is appreciable reduction of both the critical temperature and the normal state conductivity at low temperatures in some portions of the circuitry. Auger measurements show no detectable trace impurities with a concentration greater than 5% in the degraded niobium. The SSM image (Figure 10*b*), taken in a small externally applied ac field at 4.2 K, shows that although most of the circuitry is superconducting, almost none of the M2 niobium level (such as the areas outlined by *black rectangles*) is, as evidenced by its lack of Meissner shielding. Such

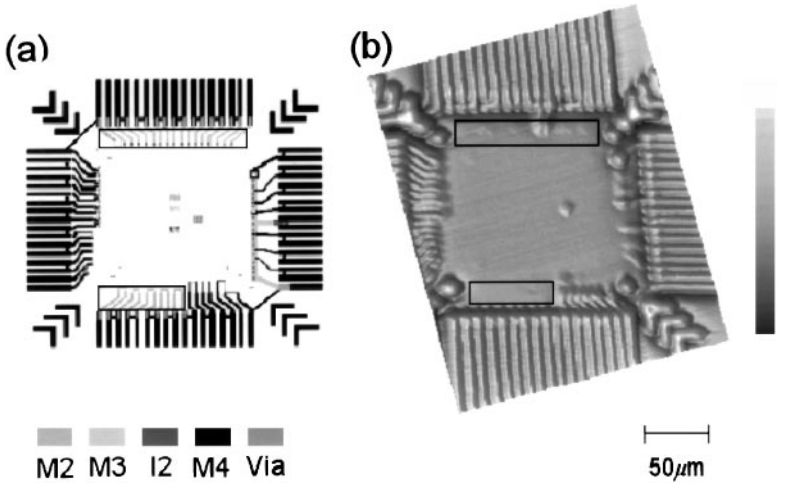

Figure 10 Schematic diagram (*a*) and SSM image (*b*) of a multilayer Nb-Al_2O_3-Nb test pattern. The M2 Nb layer in this test pattern has been exposed to an rf plasma etching step. The SQUID image shows that most of the M2 layer, for example those areas outlined by *black rectangles*, shows no screening of a small applied ac field, and is therefore not superconducting, although no damage of the layer could be seen optically, or by Auger spectroscopy.

Meissner imaging of test circuits, along with more conventional measurements, shows the conditions under which this degradation occurs. This degradation is most likely to occur when the niobium layer is not exposed by removal of an overlayer of silicon dioxide or is not surrounded by a high density of niobium circuitry. Knowing these conditions allows the development of design rules to avoid this effect.

Superconductivity: Symmetry Tests

The SSM has played a central role in phase-sensitive tests of the symmetry of the pairing of the high-T_c cuprate superconductors (89–92). In conventional superconductors the pairing of electrons is symmetric or *s*-wave. There is now overwhelming evidence that the pairing in the cuprates has $d_{x^2-y^2}$ or *d*-wave symmetry. A *d*-wave superconductor has four sign changes in the pairing wave-function as a function of momentum (as indicated by the four-leaf clovers overlaid on the SQUID microscope image of Figure 11). It is believed that the pairing wave-function is aligned with the crystal axes of the cuprate superconductors. With such momentum-dependent sign changes, it is possible to design SQUIDs with Josephson junctions whose supercurrents destructively interfere at zero applied field, rather than constructively interfering, as is the case for conventional SQUIDs (93). The first phase-sensitive symmetry tests measured the interference patterns of such specially constructed SQUIDs (89, 90). However, these experiments were subject to complications because of the self-fields generated by the currents used to measure the interference patterns and by possible spurious effects from trapped flux.

A second class of phase-sensitive experiment that does not have these complications (91, 92) employs the SSM. Figure 11 is a SSM image of four thin film, 58 μm diameter rings of the high-T_c cuprate superconductor $YBa_2Cu_3O_{7-\delta}$ (YBCO) epitaxially grown on a tricrystal substrate of $SrTiO_3$. The tricrystal geometry was chosen such that the ring at the tricrystal point has an odd number of sign changes to the component of the pairing wave function normal to the grain boundaries as it circles the tricrystal point, for a *d*-wave superconductor. The grain boundaries act like Josephson junctions. It costs energy for the superconducting wave-function to change sign across a Josephson junction. This high-energy or frustrated state is relaxed by spontaneously generating a supercurrent around the ring. For frustrated rings with sufficiently high critical current junctions, the amount of flux threading the ring is a half-integer multiple of the superconducting flux quantum [$(n + 1/2)\Phi_0$, n an integer]. The SQUID image of Figure 11 is of the sample cooled in zero field. The three outer control rings, which are not frustrated, have no flux trapped in them; the central frustrated ring has spontaneously generated flux totalling exactly half of a flux quantum. A number of experiments with different SQUID geometries have

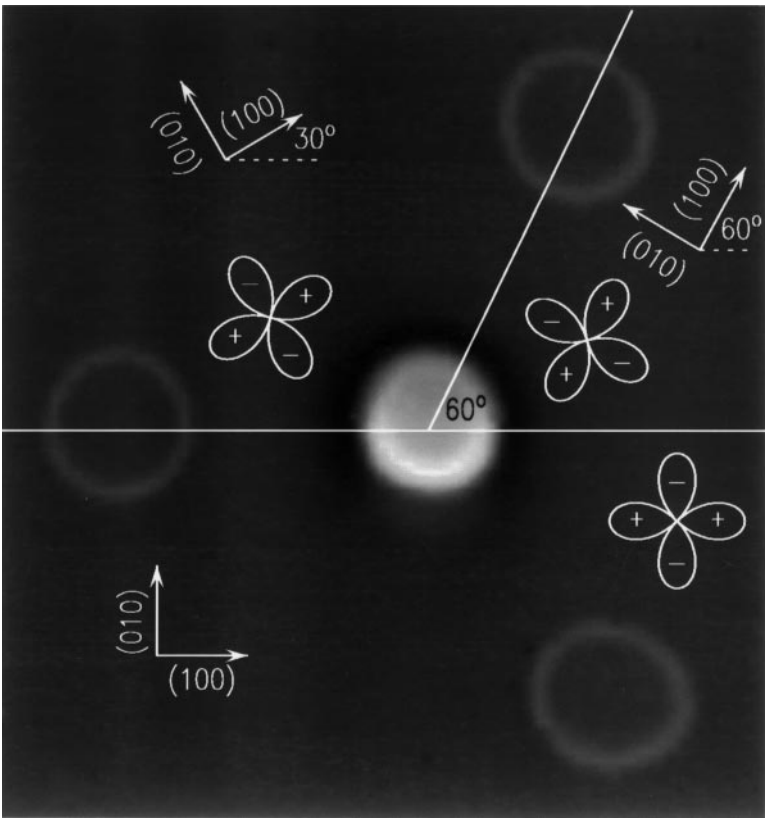

Figure 11 SSM image of four thin film rings of the high-T_c superconductor $YBa_2Cu_3O_7$ (YBCO) epitaxially grown on a specially designed tricrystal substrate of $SrTiO_3$. This image shows that the central ring spontaneously generates exactly half of a superconducting flux quantum upon cooling through the superconducting transition, whereas the outer control rings have no magnetic flux in them. This indicates that YBCO is a *d*-wave superconductor (adapted from Reference 91).

been consistent with the order parameter in YBCO having *d*-wave symmetry (94, 95).

Even an unpatterned film of a *d*-wave superconductor will generate a half-flux quantum at the tricrystal point in a frustrated geometry (96). In this case the circulating supercurrents form a Josephson vortex, so-called because the spatial extent of the magnetic field penetration along the grain boundary is set by the strength of the Josephson supercurrents across the grain boundary. The ability to do symmetry tests without patterning the films enabled the rapid demonstration that a number of the high-T_c cuprates have *d*-wave symmetry (97).

In addition, modeling of vortices trapped in the grain boundary provides a direct measurement of the Josephson penetration depth. An example of such a determination is shown in Figures 12 and 13. Figure 12 shows images of (*a*) a conventional vortex trapped in the film away from the grain boundaries; (*b*) a Josephson vortex trapped along the diagonal grain boundary, with total flux Φ_0; (*c*) a Josephson vortex trapped along the horizontal grain boundary, with total flux Φ_0, and (*d*) a Josephson vortex spontaneously generated at the tricrystal point, with a total flux of $\Phi_0/2$. The London penetration depth, which determines the extent of the spreading of the Abrikosov vortex in all directions in the plane of the film, and the extent of the spreading of the Josephson vortices perpendicular to the grain boundaries, is about 0.16 μm in YBCO, much shorter than the 4 μm diameter of the pickup loop used in these experiments. Therefore the apparent spread of the vortices in these directions is due to the finite size of the pickup loop. The Abrikosov vortex is asymmetric because of flux focusing effects from the pickup loop leads. The Josephson penetration depth can be determined for each of the grain boundaries by fitting the data to theory (96). The results, shown in Figure 13, not only confirm that the Josephson vortex at the tricrystal point has a total integrated flux which is half that of the other vortices, but also show that the Josephson penetration depth in this sample is about 2 μm for the diagonal grain boundary and about 5 μm for the horizontal grain boundary. Such local measurements may help to understand why, for example, the Josephson critical current density for such grain boundaries decreases exponentially with the grain boundary misorientation angle.

Superconductivity: Interlayer Josephson Vortices

The high critical current cuprate superconductors are highly anisotropic, with conductivities parallel to the copper-oxygen planes much higher than perpendicular to the planes. The supercurrent density normal to the planes is difficult to measure in the presence of the very large in-plane supercurrent density. This quantity is of interest for a number of reasons. For example, its size is a test of the interlayer tunneling model (98) of the origin of the superconductivity in the high-T_c superconductors. Imaging superconducting vortices trapped parallel to the planes with the SSM is a direct way of measuring the interlayer supercurrent density. A summary of some of these measurements is shown in Figure 14. This shows interlayer vortices emerging parallel to the planes from single crystals of a number of layered superconductors: (*a*) $La_2SrCu_4O_4$(La214) (JR Kirtley, KA Moler, M Nohara, T Takagi, unpublished data), (*b*) (Hg,Cu)$Ba_2CuO_{4+\delta}$(Hg1201) (100), (*c*) $Tl_2Ba_2CuO_{8+\delta}$(T12201) (101), and (*d*) the organic superconductor κ-(BEDT-TTF)$_2$Cu(NCS)$_2$ (JR Kirtley, KA Moler, JM Williams, JA Schlueter, unpublished data). In each case

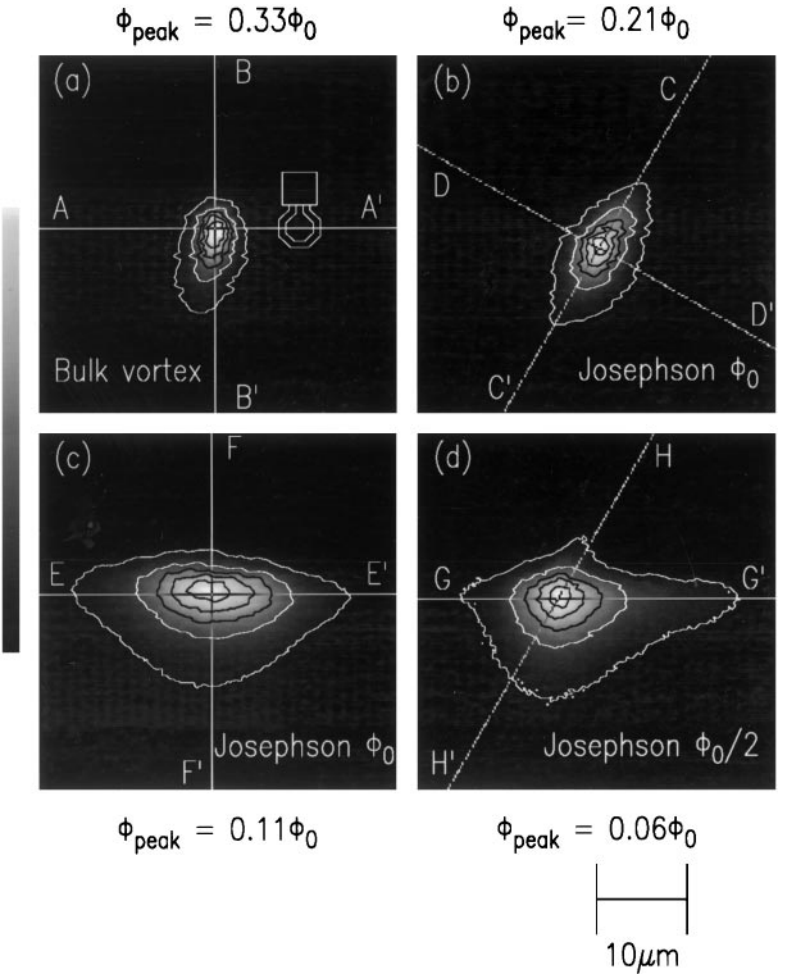

Figure 12 SSM image of superconducting vortices trapped in an unpatterned film of YBCO epitaxially grown on a tricrystal substrate of $SrTiO_3$ designed to exhibit the half-integer flux quantum effect for a *d*-wave superconductor. (*a*) A vortex trapped away from the grain boundaries. (*b*) A h/2e Josephson vortex trapped in the diagonal grain boundary. (*c*) A h/2e Josephson vortex trapped in the horizontal grain boundary. (*d*) A h/4e half-flux quantum Josephson vortex trapped at the tricrystal point. The image was taken with an octagonal pickup loop 4 μm in diameter [indicated schematically to scale in (*a*)] (adapted from Reference 96).

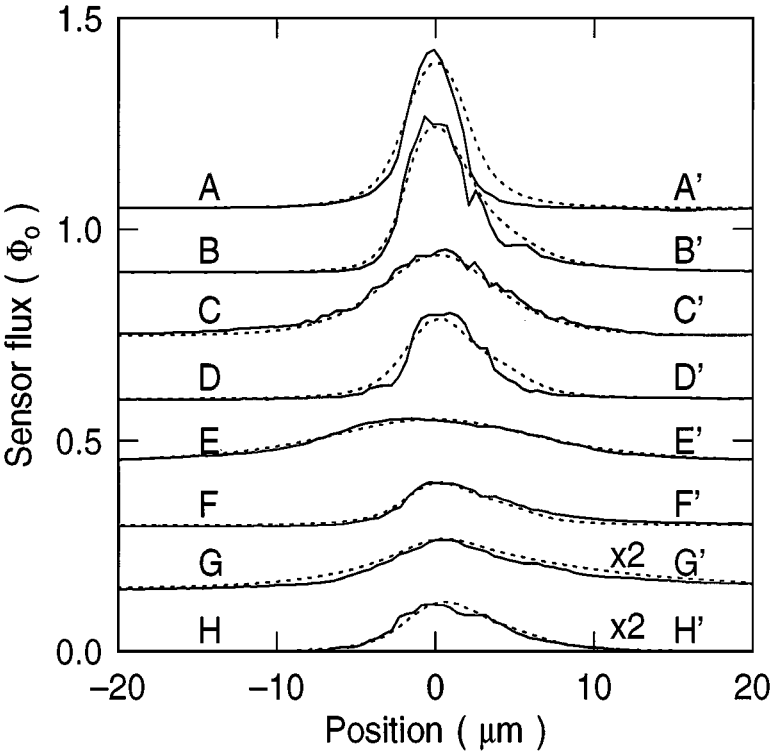

Figure 13 Fits of cross-sections through the data of Figure 12. Such modeling shows that Figure 12*d* is the image of a half-flux quantum vortex and also gives values for the Josephson penetration depths along the grain boundaries (adapted from Reference 96).

the images are oriented so the copper-oxygen planes are vertical and coming out of the plane of the figure. Overlays on each panel show a scaled schematic diagram of the pickup loop used. The images are resolution limited perpendicular to the planes. The insets in Figures 13*a*,*c* show resolution-limited vortices emerging perpendicular to the planes for 4 and 8.2 μm pickup loops, respectively. The images are not resolution limited parallel to the planes. Fitting these images to the expected magnetic fields for a vortex emerging from an anisotropic vortex (JR Kirtley, VC Kogan, JR Clem, KA Moler, unpublished data) gives values for the penetration depths parallel to the layers given in Figure 14. The values obtained for the single-layer cuprate superconductors Hg1201 and T12201 are much larger than predicted by the interlayer tunneling model, making it appear unlikely that this is the correct model for the origin of high-temperature superconductivity.

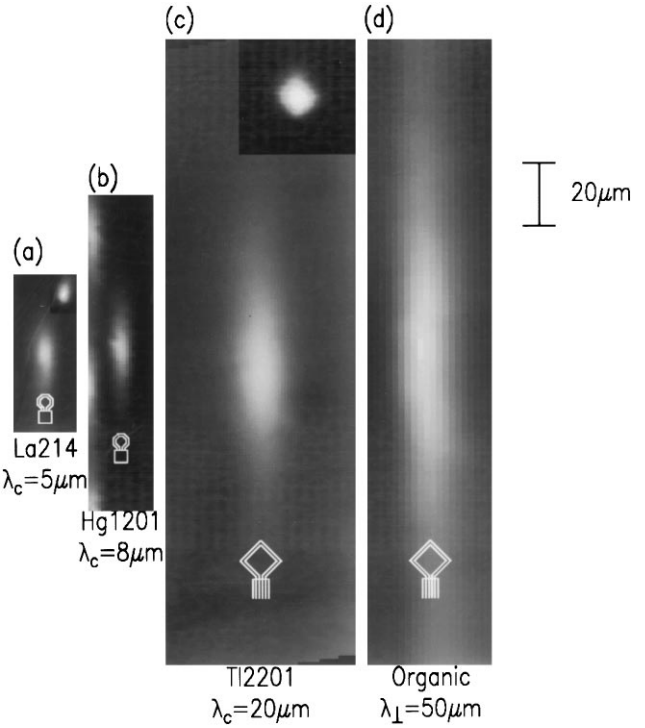

Figure 14 SSM images of vortices trapped parallel to the planes in single crystals of (*a*) $La_2SrCu_4O_4$ (99); (*b*) $(Hg,Cu)Ba_2CuO_{4+\delta}$ (100); (*c*) $Tl_2Ba_2CuO_{6+\delta}$ (101); and (*d*) the organic superconductor κ-$(BEDT\text{-}TTF)_2Cu(NCS)_2$ (102). Images (*a*) and (*b*) were taken with a 4 μm diameter octagonal SQUID pickup loop; images (*c*) and (*d*) were taken with a square pickup loop 8.2 μm on a side. The images are labeled with interlayer Josephson penetration depths obtained from fitting this data to the theory of Reference 103. Scaled schematics of the pickup loops used to image each panel are overlaid on each panel. Images of resolution limited vortices emerging perpendicular to the planes are shown as inserts in (*a*) and (*c*).

CONCLUSION

Scanning SQUID microscopes provide a powerful means to measure weak magnetic fields with spatial resolutions from microns to millimeters and larger. The appeal of this approach stems from the combination of sensitivity, spatial resolution, frequency response, linearity, dynamic range, and stability that is unique to SQUIDs, but this must be balanced by the economic and practical cost of the required cryogenic technology. For some applications, particularly those involving superconducting samples, the SQUID appears ideally suited

because of the sensitivity, spatial resolution, and its ability to be placed in close proximity to a superconducting sample. For measurements of bioelectric and corrosion currents, the sensitivity of the SQUID, particularly at low frequencies, is of paramount importance. For other studies, the intersections between the capabilities and limitations of the SQUID, those of the competing technologies, and the requirements of a particular measurement are less well defined; for example the magnetic force microscope (MFM) offers higher spatial resolution and lower sensitivity, such that the MFM would be best for some applications, and the SQUID for others. The development of a HTS SSM for the mapping of fault currents in semiconductor circuits places SQUID microscopes, for the first time, within reach of materials scientists who otherwise would not have access to a SQUID. Given the existence of a turn-key, refrigerator-cooled SQUID microscope that can be operated by nonspecialists (37), we can now look forward to a vigorous and competitive exploration of SQUID microscopy for materials science.

ACKNOWLEDGMENTS

Preparation of this manuscript was funded in part by grants from the Air Force Office of Scientific Research and the National Science Foundation. We thank M Bhushan for providing the sample shown in Figure 10, and M Nohara and H Takagi for providing the single crystal of La-214 imaged in Figure 14.

Literature Cited

1. Chang AM, Hallen HD, Harriott L, Hess HF, Kao HL, et al. 1992. *Appl. Phys. Lett.* 61:1974–76
2. Yamamoto SY, Schultz S. 1996. *Appl. Phys. Lett.* 69:3263–65
3. Rugar D, Mamin HJ, Guethner P, Lambert SE, Stern JE, et al. 1990. *J. Appl. Phys.* 68:1169–83
4. Gotoh S, Koshizuka N. 1991. *Phys. C* 176: 300–16
5. Scheinfein MR, Unguris J, Kelley MH, Pierce DT, Celotta RJ. 1990. *Rev. Sci. Instrum.* 61:2501–26
6. Harada K, Matsuda T, Bonevich J, Igarashi M, Kondo S, et al. 1992. *Nature* 360: 51–53
7. Howells G, Prance RJ, Clark TD, Prance H. 1997. *Meas. Sci. Tech.* 8:734–37
8. Bishop DJ, Gammel PL, Huse DA, Murray CA. 1992. *Science* 255:165–72
9. Oral A, Bending SJ, Humphreys RG, Henini M. 1996. *J. Low. Temp. Phys.* 105: 1135–40
10. Beardsley IA. 1989. *IEEE Trans. Mag.* 671–77
11. Weinstock H, ed. 1996. *SQUID Sensors: Fundamentals, Fabrication, and Applications.* Netherlands: Kluwer. 703 pp.
12. Weinstock H, Nisenhoff M, eds. 1989. *Superconducting Electronics.* New York: Springler-Verlag. 441 pp.
13. Wikswo JP Jr. 1995. *IEEE Trans. Appl. Supercond.* 5:74–121
14. Vu LN, Van Harlingen DJ. 1993. *IEEE Trans. Appl. Supercond.* 3:1918–21
15. Kirtley JR, Ketchen MB, Tsuei CC, Sun JZ, Gallagher WJ, et al. 1995. *IBM J. Res. Dev.* 39:655–67
16. Wellstood FC, Gim Y, Amar A, Black RC, Mathai A. 1996. *IEEE Trans. Appl. Supercond.* 7:3134–38

17. Wikswo JP Jr. 1996. See Ref. 11, pp. 307–60
18. Jenks WG, Sadeghi SSH, Wikswo JP Jr. 1997. *Phys. D* 30:293–323
19. Josephson BD. 1962. *Phys. Lett.* 1:251–53
20. Jaklevic RC, Lambe J, Silver AH, Mercereau JE. 1964. *Phys. Rev. Lett.* 12:159–60
21. Zimmerman JE, Silver AH. 1964. *Phys. Lett.* 10:47–48
22. Jaklevic RC, Lambe J, Mercereau JE, Silver AH. 1965. *Phys. Rev.* 140:A1628–37
23. Clarke J. 1989. *Proc. IEEE* 77:1208–23
24. Jenks WG, Thomas IM, Wikswo JP Jr. 1997. In *Encyclopedia of Applied Physics*, ed. GL Trigg, ES Vera, W Greulich, 19:457–68. New York: VCH
25. Koch H, Cantor R, Drung D, Erne SN, Matthies KP, et al. 1991. *IEEE Trans. Mag.* 27:2793–96
26. Black RC, Wellstood FC, Dantsker E, Miklich AH, Koelle D, et al. 1995. *IEEE Trans. Appl. Supercond.* 5:2137–41
27. Black RC, Wellstood FC, Dantsker E, Miklich AH, Nemeth DT, et al. 1995. *Appl. Phys. Lett.* 66:99–101
28. Black RC, Wellsood FC, Dantsker E, Miklich AH, Koelle D, et al. 1995. *Appl. Phys. Lett.* 66:1267–69
29. Chatraphorn S, Fleet EF, Black RC, Wellstood FC. 1998. *Appl. Phys. Lett.* 73:984–86
30. Black RC. 1995. *Magnetic microscopy using a superconducting quantum interference device (YBCO).* PhD thesis. Univ. Maryland. 302 pp.
31. Lee TS, Dantsker E, Clarke J. 1996. *Rev. Sci. Instrum.* 67:4208–15
32. Lee TS, Chemla YR, Dantsker E, Clarke J. 1997. *IEEE Trans. Appl. Supercond.* 7: 3147–50
33. Baudenbacher F, Peters N, Jenks WG, Wikswo JP Jr. 1999. *Rev. Sci. Instrum.* Submitted
34. Pitzius P, Dworak V, Hartmann U. 1999. *Appl. Supercond.* In press
35. Tavrin Y, Siegel M. 1997. *Proc. Appl. Supercond. Conf., The Netherlands, Inst. Phys. Conf. Ser.* No. 158:719–22
36. Buchanan DS, Crum DB, Cox D, Wikswo JP Jr. 1990. In *Advances in Biomagnetism*, ed. SJ Williamson, M Hoke, G Stroink, M Kotani, pp. 677–79. New York: Plenum
37. Magma-C1^{TM} Scanning HTS SQUID Microscope, Neocera, Inc., 10000 Virginia Manor Road, Beltsville, MD 20705 [*U.S. Patent No. 5491411*]
38. Anderberg J, Colclough MS. 1994. *Bull. Am. Phys. Soc.* 39(1)196 (Abstr.)
39. Black RC, Mathai A, Wellstood FC. 1993. *Appl. Phys. Lett.* 62(17):2128–30
40. Black RC, Wellstood FC, Ludwig F, Koelle D, Nemeth DT, et al. 1994. *Bull. Am. Phys. Soc.* 39(1):523 (Abstr.)
41. Kirtley JR, Ketchen MB, Chaudhari P, Khare N, Stawiasz KG. 1994. *Bull. Am. Phys. Soc.* 39(1):222 (Abstr.)
42. Mathai A, Song D, Gin Y, Wellstood FC. 1993. *IEEE Trans. Appl. Supercond.* 3: 2609–12
43. Vu LN, Wistrom MS, Van Harlingen DJ. 1993. *Appl. Phys. Lett.* 63:1693–95
44. Kirtley JR, Ketchen MB, Stawiasz KG, Sun JZ, Gallagher WJ, et al. 1995. *Appl. Phys. Lett.* 66(9):1138–40
45. Jeffery M, Van Duzer T, Kirtley JR, Ketchen MB. 1995. *Appl. Phys. Lett.* 67: 1769–72
46. Dechert J, Krischker K, Göddenhenrich T, Mück M, Heiden C. 1997. *IEEE Trans. Appl. Supercond.* 7:3143–46
47. Siegel J, Witt J, Venturi N, Field SB. 1995. *Rev. Sci. Instrum.* 66:2520–23
48. Wikswo JP Jr. 1988. *Adv. Cryo. Eng.* 3: 107–16
49. Wikswo JP Jr, Roth BJ. 1988. *Electroencep. Clin. Neurophysiol.* 69:266–76
50. Roth BJ, Sepulveda NG, Wikswo JP Jr. 1989. *J. Appl. Phys.* 65:361–72
51. Tan S, Roth BJ, Wikswo JP Jr. 1990. *Electroencep. Clin. Neurophysiol.* 76:73–85
52. Tan S. 1992. *Linear system imaging and its applications to magnetic measurements by SQUID magnetometers.* PhD thesis. Vanderbilt Univ. 227 pp.
53. Tan S, Ma YP, Thomas IM, Wikswo JP Jr. 1993. *IEEE Trans. Appl. Supercond.* 3:1945–48
54. Staton DJ. 1994. *Magnetic imaging of applied and propagating action currents in cardiac tissue slices: determination of anisotropic electrical conductivities in a two-dimensional bidomain.* PhD thesis. Vanderbilt Univ. 147 pp.
55. Tan S, Sepulveda NG, Wikswo JP Jr. 1995. *J. Comput. Phys.* 122:150–64
56. Roth BJ, Wikswo JP Jr. 1990. *Rev. Sci. Instr.* 61:2439–48
57. Wikswo JP Jr. 1996. See Ref. 11, pp. 629–95
58. Wikswo JP Jr, Ma YP, Sepulveda NG, Tan S, Thomas IM, Lauder A. 1993. *IEEE Trans. Applied Supercond.* 3:1995–2002
59. Thomas IM, Moyer TC, Wikswo JP Jr. 1992. *Geophys. Res. Lett.* 19:2139–42
60. Weinstock H, Erber T, Nisenoff M. 1985. *Phys. Rev. B* 31:1535–52
61. Ma YP, Wikswo JP Jr. 1998. *Rev. Prog. Quantitative NDE* 17A:1067–74

62. Wikswo JP Jr, Crum DB, Henry WP, Ma YP, Sepulveda NG, et al. 1993. *J. Nondestr. Eval.* 12:109–19
63. Staton DJ, Rousakov SV, Wikswo JP Jr. 1996. *Rev. Prog. Quantitative NDE* 15: 845–51
64. Black RC, Wellstood FC. 1994. *Appl. Phys. Lett.* 64:100–2
65. Weinstock H, Trashawala N, Claycombe JR, Shaw TJ, Clarke J. 1999. *Rev. Prog. Quantitative NDE* 18: In press
66. Wikswo JP Jr. 1997. *NACE Int.* 293:1–17
67. Bellingham JG, MacVicar MLA, Nisenoff M, Searson PC. 1986. *J. Electrochem. Soc.* 133:1753–54
68. Bellingham JG, MacVicar MLA, Nisenoff M. 1987. *IEEE Trans. Mag.* 23(2): 477–79
69. Jette BD, MacVicar MLA. 1991. *IEEE Trans. Mag.* 27:3025–28
70. Misra M, Lordi S, MacVicar MLA. 1991. *IEEE Trans. Mag.* 27:3245–48
71. Hibbs AD, Sager RE, Cox DW, Aukerman TH, Sage TA, et al. 1992. *Rev. Sci. Instrum.* 63(7):3652–58
72. Hibbs AD. 1992. *J. Electrochem. Soc.* 139(9):2447–57
73. Hibbs AD, Chung R, Pence JS. 1994. *Rev. Prog. Quantitative NDE* 13:1955–62
74. Richter H, Knecht A. 1997. *Materialpruefung* 39:390–96
75. Li D, Ma YP, Flanagan WF, Lichter BD, Wikswo JP Jr. 1994. *Proc. Tri-Service Conf. Corrosion, Orlando, FL.* 335–46
76. Li D, Ma YP, Flanagan WF, Lichter BD, Wikswo JP Jr. 1995. *J. Min. Met. Mater.* 47:36–39
77. Li D, Ma YP, Flanagan WF, Lichter BD, Wikswo JP Jr. 1996. *Corrosion* 52:219–31
78. Li D, Ma YP, Flanagan WF, Lichter BD, Wikswo JP Jr. 1997. *Corrosion* 53:93–98
79. London F. 1948. *Phys. Rev.* 74:562–73
80. Deaver BS, Fairbank WM. 1961. *Phys. Rev. Lett.* 7:43–46
81. Doll R, Näbauer M. 1961. *Phys. Rev. Lett.* 7:51–52
82. Zimmerman JE, Mercereau JE. 1964. *Phys. Rev. Lett.* 13:125–26
83. Goodman WL, Deaver BS Jr. 1970. *Phys. Rev. Lett.* 24:870–73
84. Goodman WL, Willis WD, Vincent DA, Deaver BS Jr. 1970. *Phys. Rev. B* 4:1530–38
85. Pierce JM. 1970. *Phys. Rev. Lett.* 24:874–76
86. Rogers FP. 1983. *A device for experimental observation of flux vortices trapped in superconducting thin films.* MS thesis. Massachusetts Institute of Technology. 100 pp.
87. Scott BA, Kirtley JR, Walker D, Chen BH, Wang H. 1997. *Nature* 389:164–67
88. Deleted in proof
89. Wollman DA, Van Harlingen DJ, Lee WC, Ginsberg DM, Leggett AJ. 1993. *Phys. Rev. Lett.* 71:2134–37
90. Brawner DA, Ott HR. 1994. *Phys. Rev. B* 50:6530–33
91. Tsuei CC, Kirtley JR, Chi CC, Yu-Jahnes LS, Gupta A, et al. 1994. *Phys. Rev. Lett.* 73:593–96
92. Mathai A, Gim Y, Black RC, Amar A, Wellstood FC. 1995. *Phys. Rev. Lett.* 74: 4523–26
93. Sigrist M, Rice TM. 1992. *J. Phys. Soc. Jpn.* 61:4283–86
94. Kirtley JR, Tsuei CC, Sun JZ, Chi CC, Yu-Jahnes LS, et al. 1995. *Nature* 373:225–28
95. Gim Y, Mathai A, Black R, Amar A, Wellstood FC. 1997. *IEEE Trans. Appl. Supercond.* 7:2331–34
96. Kirtley JR, Tsuei CC, Rupp M, Sun JZ, Yu-Jahnes LS. 1996. *Phys. Rev. Lett.* 76: 1336–39
97. Kirtley JR, Tsuei CC, Moler KA, Sun JZ, Gupta A, et al. 1996. *Czech J. Phys.* 46:S6:3169–76 (Suppl.)
98. Wheatley J, Hsu T, Anderson PW. 1988. *Nature* 333:121–21
99. Deleted in proof
100. Kirtley JR, Moler KA, Villard G, Maignan A. 1998. *Phys. Rev. Lett.* 81:2140–43
101. Moler KA, Kirtley JR, Hinks DG, Li TW, Xu M. 1998. *Science* 279:1193–96